



**University of  
Sunderland**

Hu, Ning, Zemba, Y, Okabe, T, Yan, C, Fukunaga, Hisao and Elmarakbi, Ahmed (2008) A new cohesive model for simulating delamination propagation in composite laminates under transverse loads. *Mechanics of Materials*, 40 (11). pp. 920-935. ISSN 0167-6636

Downloaded from: <http://sure.sunderland.ac.uk/id/eprint/1646/>

#### **Usage guidelines**

Please refer to the usage guidelines at <http://sure.sunderland.ac.uk/policies.html> or alternatively contact [sure@sunderland.ac.uk](mailto:sure@sunderland.ac.uk).





## A new cohesive model for simulating delamination propagation in composite laminates under transverse loads

N. Hu<sup>a,b,\*</sup>, Y. Zemba<sup>b</sup>, T. Okabe<sup>b</sup>, C. Yan<sup>c</sup>, H. Fukunaga<sup>b</sup>, A.M. Elmarakbi<sup>d</sup>

<sup>a</sup> Department of Engineering Mechanics, Chongqing University, Chongqing 400030, PR China

<sup>b</sup> Department of Aerospace Engineering, Tohoku University, 6-6-01 Aramaki-Aza-Aoba, Aoba-ku, Sendai 980-8579, Miyagi, Japan

<sup>c</sup> School of Engineering Systems, Queensland University of Technology, 2 George Street, GPO Box 2434, Brisbane, Qld 4001, Australia

<sup>d</sup> School of Computing and Technology, University of Sunderland, Sunderland SR6 0DD, United Kingdom

### ARTICLE INFO

#### Article history:

Received 20 April 2007

Received in revised form 6 May 2008

#### Keywords:

Cohesive interface model

Laminate

Delamination

Finite element analysis

Transverse loads

In-plane damages

### ABSTRACT

In this paper, we propose a new cohesive model to stably and accurately simulate the delamination propagations in composite laminates under quasi-static and low-velocity impact transverse loads using comparatively *coarse meshes*. In this model, a *pre-softening zone* ahead of the existing traditional softening zone is proposed. In this pre-softening zone, the initial stiffnesses and the interface strengths at the integration points of cohesive elements are gradually reduced as the corresponding effective relative displacements at these points increase. However, the onset displacement corresponding to the onset damage is not changed in this model. Moreover, the fracture toughness of materials for determining the final displacement of complete decohesion is kept constant. This cohesive model is implemented in the explicit time integration scheme combined with a powerful three-dimensional (3D) hybrid finite element for evaluating the delamination propagations on interfaces in composite laminates. A DCB problem is employed to analyze the characteristics of the present cohesive model. In order to reduce the computational cost for dealing with more complex problems, a stress-based criterion is also adopted in our numerical model for evaluating various in-plane damages, such as matrix cracks, fiber breakage, etc. Finally, two experimental examples are employed to illustrate the validity of the present approach.

© 2008 Elsevier Ltd. All rights reserved.

### 1. Introduction

It is well-known that very complicated damage phenomena occur in composite laminated structures under transverse loads. Understanding the mechanisms of the happening and propagation of the damages is crucial for properly designing this kind of structures. Generally, there are two main categories in various damages in composite laminates under the transverse loads. The first category consists of various in-plane damages, such as fiber failure,

transverse matrix cracking, etc. The second category includes the interface damages, i.e. delaminations among multiple laminae, which are the dominant damages of laminates.

So far, a lot of research has been conducted to experimentally or numerically investigate the damage phenomena of composite laminates under the transverse loads. In the following, only the studies in the field of theoretical models and numerical simulations are briefly reviewed. For various in-plane damages, various stress-based criteria have been put forward. For instance, Chang and Chang (1987) and Hou et al. (2000) proposed the tension-shear failure criteria for matrix cracking. In these criteria, the damage conditions relate to single ply failure, which are not unique, but have a great degree of commonality with

\* Corresponding author. Address: Department of Aerospace Engineering, Tohoku University, 6-6-01 Aramaki-Aza-Aoba, Aoba-ku, Sendai 980-8579, Miyagi, Japan. Tel.: +81 22 795 4109/6994; fax: +81 22 795 4109.  
E-mail address: [hu@ssl.mech.tohoku.ac.jp](mailto:hu@ssl.mech.tohoku.ac.jp) (N. Hu).

other widely accepted criteria. Also, to predict the delaminations in laminates, some stress-based criteria have been proposed. For instance, Brewer and Lagace (1988) proposed a delamination criterion. Hou et al. (2001) further modified this delamination criterion by taking into account the interaction between the out-of-plane compression and interlaminar shear. From many previous studies, it has been concluded that the stress-based criteria are effective to predict the initiation of various damages, especially for in-plane damages, such as fiber failure and matrix cracking. However, there has been much debate on that using the stress-based criteria to simulate damage propagation process, especially for delamination extension. As pointed out by Davies and Zhang (1995), in the stress-based criteria for delamination, the scale effects would not be exhibited as in a fracture model. Therefore, it may be inaccurate to use them to predict the delamination size or model the delamination propagation. It almost certainly requires an energy release rate algorithm based on the knowledge of fracture mechanics.

To understand the mechanism of the delaminations occurring on the interfaces of different layers, besides the above stress-based criteria, some methods based on fracture mechanics have also been proposed. For instance, Zheng and Sun (1995) and Li et al. (2002a,b) directly evaluated the strain energy released rate of the mixed-mode at the delamination front for modeling the delamination propagation. However, this kind of methods cannot deal with the initiation of delaminations, therefore, some initial pre-existing small delamination areas must be assumed. Furthermore, various cohesive interface models, which can tackle the initiation and propagation of crack or delamination simultaneously, are widely used due to their inherent simplicity and efficiency (Xu and Needleman, 1994; Camacho and Ortiz, 1996; Geubelle and Baylor, 1998; Reddy et al., 1997; Mi et al., 1998; Goncalves et al., 2000; Camanho and Davila, 2002; Segurado and Llorca, 2004; Nishikawa et al., 2007). However, when using cohesive elements to simulate the interface damage propagations, such as delamination propagation, there are two main problems. The first one is the numerical instability problem as pointed out by Mi et al. (1998), Goncalves et al. (2000), Gao and Bower (2004) and Hu et al. (2007a). This problem is caused by a well-known elastic snap-back instability, which occurs just after the stress reaches the peak strength of the interface. Especially for those interfaces with high strength and high initial stiffness, this problem becomes more obvious when using comparatively coarse meshes (Hu et al., 2007a). Traditionally, this problem can be controlled using some direct techniques. For instance, a very fine mesh can alleviate this numerical instability, however, which leads to very high computational cost. Also, very low interface strength and the initial interface stiffness in the whole cohesive area can partially remove this convergence problem, which, however, lead to the lower slope of loading history in the loading stage before the happening of damages. Furthermore, various generally oriented methodologies can be used to remove this numerical instability, e.g. Riks method (Riks, 1979) which can follow the equilibrium path after instability. Recently, the artificial damping method with additional energy dissipations has been

proposed by Gao and Bower (2004). Also, the present authors proposed a kind of move-limit method (Hu et al., 2007a) to remove the numerical instability using cohesive model for delamination propagation. In this technique, the move-limit in the cohesive zone provided by artificial rigid walls is built up to restrict the displacement increments of nodes in the cohesive zone of laminates after delaminations occurred. Therefore, similar to the artificial damping method (Gao and Bower, 2004), the move-limit method introduces the artificial external work to stabilize the computational process. As shown later, although these methods (Gao and Bower, 2004; Hu et al., 2007a) can remove the numerical instability when using comparatively coarse meshes, the second problem occurs, which is the error of peak load in the load–displacement curve. The numerical peak load is usually higher than the real one as observed by Goncalves et al. (2000) and Hu et al. (2007a).

With the previous background in mind, the objective of this paper is to propose a new cohesive model named as adaptive cohesive model (ACM), for stably and accurately simulating delamination propagations in composite laminates under transverse quasi-static or impact loads when using comparatively *coarse cohesive elements* in order to reduce the computational cost. In this model, ahead of the existing softening zone located at the delamination tip, we propose a *pre-softening zone*. In this pre-softening zone, with the increase of effective relative displacements at the integration points of cohesive elements on interfaces, the initial stiffnesses and interface strengths at these points are reduced gradually. However, the onset displacement for starting the real softening process is not changed in this model. The critical energy release rate or fracture toughness of materials for determining the final displacement of complete decohesion is kept constant. In the pre-softening zone, the lower limit of the interface strength and stiffness can be theoretically estimated according to the mesh size. This cohesive model is implemented in the explicit time integration scheme combined with a powerful 3D eight-noded hybrid brick element (Cao et al., 2002) for evaluating the delamination propagations in composite laminates. A DCB problem is employed to analyze the properties of the present ACM. We found that this model can effectively remove the numerical instability and errors in the peak loads for coarse meshes. Moreover, to deal with more complex damage phenomena in composite laminates with lower computational cost, a stress-based criterion by Hou et al. (2000) is adopted to tackle various in-plane damages at the integration points within individual 3D brick element. The strategy for updating the in-plane stiffness due to various in-plane damages in our previous work (Hu et al., 2007a) is adopted. Then, two categories of damage patterns in composite structures under transverse loads, i.e. delaminations and in-plane damages are tackled independently. Finally, this numerical simulation method is applied for more complex problems, such as GFRP and CFRP laminated plates under transverse quasi-static or impact loads. The corresponding experimental results are employed to validate the present method. It is shown that the present method can successfully simulate the complex damage behaviors of laminates under transverse loads with lower computational cost.

## 2. Theory of cohesive element for interface damages

### 2.1. Theory of traditional cohesive element

To analyze the delamination propagation at interfaces in laminates, there have been a lot of proposed cohesive models in many previous studies, here a zero-thickness cohesive element with eight-nodes in Fig. 1 is adopted (Camanho and Davila, 2002) to simulate the resin-rich layer connecting the several laminae of a composite laminate, which is briefly described here for the integrity of the work.

The constitutive equation of zero-thickness cohesive elements is established in terms of relative displacements and tractions across the interface. The relative displacements for an element with a general orientation in 3D space are defined in Fig. 1. In this figure, at each integration point of cohesive element, we define the relative displacements  $\delta_s = \{\delta_1, \delta_2, \delta_3\}^T$  in local coordinates obtained from the displacement vector  $\mathbf{u} = \{u_1, u_2, u_3\}^T$  in the global coordinates as follows:

$$\delta_s = \mathbf{B}_s \mathbf{u} \tag{1}$$

The constitutive relationship of the cohesive element,  $\mathbf{D}_s$  at each integration point, relates the tractions,  $\tau_s$ , to the relative displacements  $\delta_s$  as

$$\tau_s = \mathbf{D}_s \delta_s \tag{2}$$

The stiffness matrix of the cohesive element can be obtained from the principle of virtual work as follows:

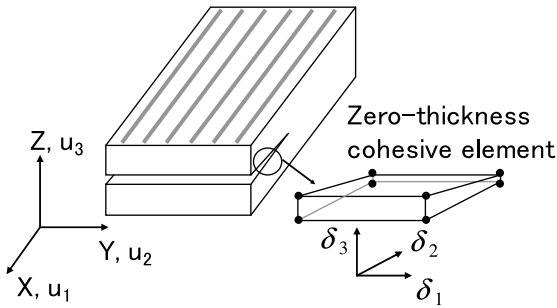


Fig. 1. Cohesive interface element.

$$\mathbf{k}_s = \int_{\Gamma} \mathbf{B}_s^T \mathbf{D}_s \mathbf{B}_s d\Gamma \tag{3}$$

The  $4 \times 4$  Newton–Cotes closed integration scheme, which can overcome the locking caused by the strong initial interface stiffness (Camanho and Davila, 2002), is adopted in this work to evaluate the stiffness matrix of cohesive element.

Here, it is a fundamental task to build up an appropriate constitutive equation in the formulation of the cohesive element for accurate simulations of the interlaminar cracking process. It is considered that there is a process zone or cohesive zone ahead of the delamination tip, which physically represents the coalescence of crazes in the resin-rich layer located at the delamination tip and reflects the way by which the material loses load carrying capacity. As shown in Fig. 2 for a bi-linear model (Camanho and Davila, 2002) in the cases of typical pure mode I, II or III, after the interfacial normal or shear tractions attain their respective interlaminar tensile or shear strengths at an integration point of the cohesive element, the stiffness of the cohesive element at this point is gradually reduced to zero. The softening onset displacements are obtained as

$$\delta_3^0 = N/K, \quad \delta_2^0 = S/K, \quad \delta_1^0 = T/K \tag{4}$$

where  $N, S$  and  $T$  are the interlaminar tensile and shear strengths, respectively, and  $K$  is the initial stiffness of interface.

The area under the traction–relative displacement curves is the respective (mode I, II, III) fracture toughness ( $G_{IC}, G_{IIC}, G_{IIIC}$ ), which is used to define the final relative displacements corresponding to complete decohesion, i.e.,  $\delta_3^f, \delta_2^f$  and  $\delta_1^f$  as

$$\int_0^{\delta_3^f} \tau_3 d\delta_3 = G_{IC}, \quad \int_0^{\delta_2^f} \tau_2 d\delta_2 = G_{IIC}, \quad \int_0^{\delta_1^f} \tau_1 d\delta_1 = G_{IIIC} \tag{5}$$

The final displacements for the state of complete decohesion are then obtained as

$$\delta_3^f = 2G_{IC}/N, \quad \delta_2^f = 2G_{IIC}/S, \quad \delta_1^f = 2G_{IIIC}/T \tag{6}$$

For the mixed-mode, the current effective relative displacement  $\delta_m$  is defined as

$$\delta_m = \sqrt{\delta_1^2 + \delta_2^2 + \langle \delta_3 \rangle^2} = \sqrt{\delta_{shear}^2 + \langle \delta_3 \rangle^2} \tag{7}$$

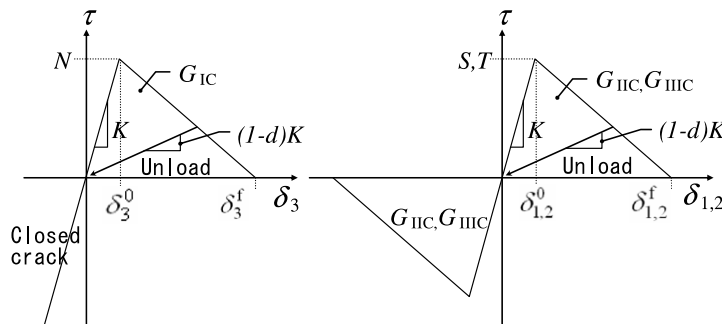


Fig. 2. Constitutive law of traditional cohesive interface element.

where  $\delta_{\text{shear}}$  represents the norm of the vector defining the tangential relative displacements of the element, and the MacCauley bracket (i.e.  $\langle \cdot \rangle$ ) is defined as

$$\langle x \rangle = \begin{cases} 0 & \leftarrow x \leq 0 \\ x & \leftarrow x > 0 \end{cases} \quad (8)$$

Assuming  $S = T$ , the single-mode relative displacements at softening onset are defined from Eq. (4) as follows:

$$\delta_3^0 = N/K, \quad \delta_1^0 = \delta_2^0 = \delta_{\text{shear}}^0 = S/K \quad (9)$$

When the opening displacement  $\delta_3$  is greater than zero, the mode mixity ratio  $\beta$  is

$$\beta = \frac{\delta_{\text{shear}}}{\delta_3} \quad (10)$$

The softening onset displacement of mixed-mode, i.e.  $\delta_m^0$ , is then defined as

$$\delta_m^0 = \begin{cases} \delta_3^0 \delta_1^0 \sqrt{\frac{1+\beta^2}{(\delta_1^0)^2 + (\beta \delta_3^0)^2}} & \leftarrow \delta_3 > 0 \\ \delta_{\text{shear}}^0 & \leftarrow \delta_3 \leq 0 \end{cases} \quad (11)$$

The final displacement of mixed-mode corresponding to the state of complete decohesion is obtained from the well-known B–K model as follows:

$$\delta_m^f = \begin{cases} \frac{2}{K_m^0} \left[ G_{IC} + (G_{IIC} - G_{IC}) \left( \frac{\beta^2}{1+\beta^2} \right)^\eta \right] & \leftarrow \delta_3 > 0 \\ \sqrt{(\delta_1^f)^2 + (\delta_2^f)^2} & \leftarrow \delta_3 \leq 0 \end{cases} \quad (12)$$

$\eta$  is chosen through the comparison with experimental results (usually it ranges from 1.3 to 1.8).

Furthermore,  $\delta_m^{\text{max}}$  is defined to be the maximum effective relative displacement of one integration point within a cohesive element in the loading history. Using the max value of the effective relative displacement rather than the current value  $\delta_m$  prevents healing of the interface. Finally, the constitutive matrix  $\mathbf{D}_s$  in Eq. (2) for mixed-mode is evaluated by the penalty parameter, i.e. initial stiffness of interface  $K$ , the damage evolution function  $d$ , and the softening onset and final displacements of mixed-mode, i.e.,  $\delta_m^0$  and  $\delta_m^f$ , respectively, as

$$\mathbf{D}_{\text{sr}} = \begin{cases} \bar{\delta}_{\text{sr}} K \leftarrow \delta_m^{\text{max}} \leq \delta_m^0 & \text{intact} \\ \bar{\delta}_{\text{sr}} [(1-d)K] \leftarrow \delta_m^0 < \delta_m^{\text{max}} < \delta_m^f & \text{and } \delta_3 > 0 \\ \bar{\delta}_{\text{sr}} [(1-d)K + Kd\bar{\delta}_{s3}] \leftarrow \delta_m^0 < \delta_m^{\text{max}} < \delta_m^f & \text{and } \delta_3 \leq 0 \\ \delta_3 \leq 0 & \text{softening} \\ 0 \leftarrow \delta_m^{\text{max}} \geq \delta_m^f & \text{and } \delta_3 > 0 \\ \bar{\delta}_{s3}\bar{\delta}_{3r}K \leftarrow \delta_m^{\text{max}} \geq \delta_m^f & \text{and } \delta_3 \leq 0 \\ \text{complete decohesion} \end{cases} \quad (13a)$$

$$d = \frac{\delta_m^f(\delta_m^{\text{max}} - \delta_m^0)}{\delta_m^{\text{max}}(\delta_m^f - \delta_m^0)}, \quad d \in [0, 1] \quad (13b)$$

where  $\bar{\delta}_{\text{sr}}$  is the Kronecker delta.

It should be noticed that the above equation avoids the interpenetration of the crack faces of the cohesive element in the state of compression for softening and complete decohesion states.

## 2.2. Adaptive cohesive model

In many previous studies (Mi et al., 1998; Gonçalves et al., 2000; Gao and Bower, 2004; Hu et al., 2007a), it was found that computations using cohesive zones to model crack nucleation often experience convergence difficulties at the point where the crack first nucleates. Various approaches (Riks, 1979; Gao and Bower, 2004; Hu et al., 2007a) can be used to resolve these convergence problems, which usually introduce the artificial external work into the original system to stabilize the computational process. Another problem is the error in the peak load of the load–displacement curve when using comparatively coarse meshes although the stable numerical simulations can be realized using these approaches. To remove the numerical instability when using the coarse meshes, as shown in Fig. 3, ahead of the traditional softening zone, we insert a transition area called as *pre-softening zone*. In this zone, the initial stiffness and interface strength of the integration points in cohesive elements are gradually reduced as  $\delta_m^{\text{max}}$  increases. In Fig. 4, the stiffness  $K$  and the interface strength, e.g.,  $N$  for mode I, are linearly updated with the increase of  $\delta_m^{\text{max}}$  as follows:

$$N_i = \frac{\delta_m^{\text{max}}}{\delta_m^0} (N_{\text{min}} - N_0) + N_0, \quad (N_0 > N_{\text{min}}) \\ \text{and } (\alpha \delta_m^0 < \delta_m^{\text{max}} < \delta_m^0) \quad (14a)$$

$$K_i = \frac{\delta_m^{\text{max}}}{\delta_m^0} (K_{\text{min}} - K_0) + K_0, \quad (K_0 > K_{\text{min}}) \\ \text{and } (\alpha \delta_m^0 < \delta_m^{\text{max}} < \delta_m^0) \quad (14b)$$

where  $N_0$  is the initial interface strength,  $N_{\text{min}}$  the lower limit of interface strength,  $K_0$  the initial stiffness and  $K_{\text{min}}$  is the lower limit of stiffness.

Note that Eq. (14a) also holds for  $S$  and  $T$  used in modes II and III. By choosing the proper ratio between the lower limits of strength and stiffness (e.g.,  $N_{\text{min}}$  and  $K_{\text{min}}$ ), from Eq. (9), the following relations can be realized easily:

$$\delta_3^0 = \frac{N_0}{K_0} = \frac{N_i(\delta_m^{\text{max}})}{K_i(\delta_m^{\text{max}})} = \frac{N_{\text{min}}}{K_{\text{min}}}, \\ \delta_2^0 = \delta_1^0 = \frac{S_0}{K_0} = \frac{S_i(\delta_m^{\text{max}})}{K_i(\delta_m^{\text{max}})} = \frac{S_{\text{min}}}{K_{\text{min}}} \quad (\text{for } S = T) \quad (15)$$

Therefore, from Eq. (11), the onset displacement  $\delta_m^0$  in the pre-softening zone is the same as that in the traditional cohesive model, which does change in the updating process of the interface stiffness and strength.

Moreover, to keep the constant fracture toughness  $G_c$  when reducing  $K$ ,  $N$  and  $S$  in Eq. (14), the final displacement  $\delta_m^f$  is adjusted correspondingly according to Eqs. (6) and (12), which is schematically shown in Fig. 4. Once the integration point enters into the *real softening process*, i.e.,  $\delta_m^{\text{max}} > \delta_m^0$ , the current values of strength and stiffness, i.e.,  $N_n$  and  $K_n$  in Figs. 3 and 4, will be constantly used in the subsequent computations. It should be noted that  $\alpha$  in Eq. (14) is a parameter to define the size of pre-softening zone. When  $\alpha = 1$ , the present ACM model degenerates into the traditional cohesive model.

In the above adaptive model,  $N_0$  can be taken as the real interface strength. Therefore, it is crucial to define  $N_{\text{min}}$

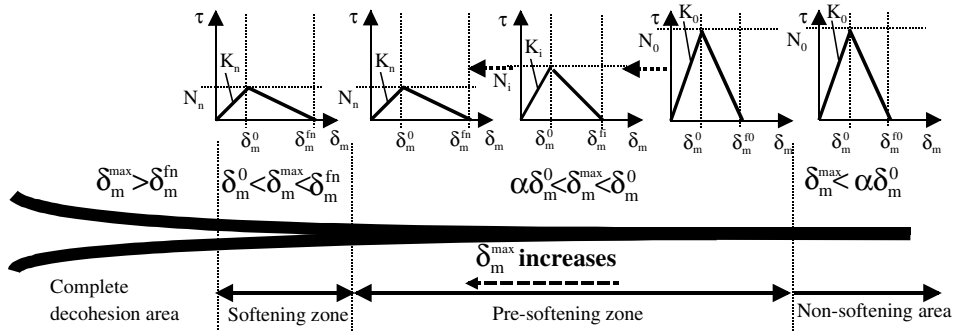


Fig. 3. Schematic view of adaptive cohesive model ( $\alpha = 0-1.0$ ).

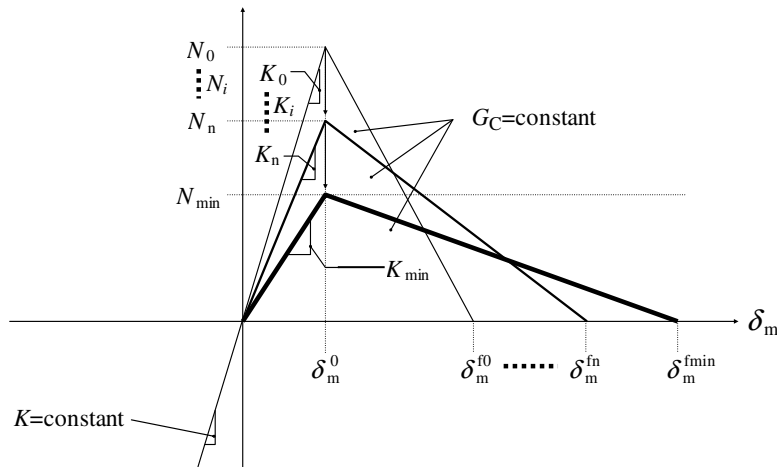


Fig. 4. Constitutive law of adaptive cohesive model.

from the consideration of computational stabilization and accuracy. Mi et al. (1998) have concluded that several elements in the softening zone are needed to realize stable numerical simulations of the interface crack propagation. Here, by referring to this statement, for instance, for the case of mode I, the size of softening zone  $R$  was defined by Geubelle and Baylor (1998) as follows:

$$R = N_c R_n = \frac{\pi E_{\text{polymer}} G_{IC}}{2(1-\nu^2) N_{\min}^2} \quad (16)$$

where  $N_c$  is the number of elements in softening zone, which ranges from 2 to 5 from our numerical experiences,  $R_n$  the element size, and  $E_{\text{polymer}}$  and  $\nu$  are the Young's modulus and Poisson's ratio of polymer.

Finally,  $N_{\min}$ , which depends on the element size, can be calculated as follows:

$$N_{\min} = \sqrt{\frac{\pi E_{\text{polymer}} G_{IC}}{2(1-\nu^2) N_c R_n}} \quad (17)$$

For the mixed-mode, the similar formulation can be set up by simply replacing  $G_{IC}$  by  $G_c$ , which is equal to  $G_{IC} + (G_{IIC} - G_{IC}) \left(\frac{\beta^2}{1+\beta^2}\right)^\eta$  from Eq. (12).

The above ACM is of the engineering meaning when using coarse meshes for complex composite structures,

which is, in fact, an 'artificial' means for achieving the stable numerical simulation process. A reasonable explanation is that all numerical techniques are artificial, whose accuracy strongly depends on their mesh sizes, especially at the front of crack tip. To remove the factitious errors in the simulation results caused by the coarse mesh sizes in the numerical techniques, we artificially adjust some material properties in order to partially alleviate or remove the numerical errors. Otherwise, we have to resort very fine meshes, which may be computationally impractical for very complex problems from the capabilities of most current computers. Of course, the modified material parameters should be those which do not have the dominant influences on the physical phenomena. For example, the interface strength usually controls the initiation of interface cracks. However, it is not crucial for determining the crack propagation process and final crack size from the viewpoint of fracture mechanics. Moreover, there has been almost no clear rule to exactly determine the interface stiffness, which is a parameter determined with a high degree of freedom in practical cases. Therefore, the effect of the modifications of interface strength and stiffness can be very small since the practically used onset displacement  $\delta_m^0$  for delamination initiation is remained constant in our model. For the parameters, which dominate the fracture

phenomena, should be unchanged. For instance, in our model, the fracture toughness dominating the behaviors of interface damages is kept constant.

### 3. Numerical verifications

#### 3.1. A DCB problem

A DCB test specimen of a  $(0^\circ)_{24}$ , T300/977-2 carbon fiber-reinforced epoxy laminate, containing a thin insert at the mid-plane near the loaded end, is simulated (Camanho and Davila, 2002). As shown in Fig. 5, this specimen is 150 mm long, 20 mm wide, with two 1.98 mm thick plies, and with an initial crack length of 55 mm. The material properties are:  $E_{11} = 150.0$  GPa,  $E_{22} = E_{33} = 11.0$  GPa,  $G_{12} = G_{13} = 6.0$  GPa,  $G_{23} = 3.7$  GPa,  $\nu_{12} = \nu_{13} = 0.25$ ,  $\nu_{23} = 0.45$  and  $\rho = 1444$  kg/m<sup>3</sup>. It is a static experiment (Camanho and Davila, 2002). As shown in Fig. 5, in our computations, the loading speed is taken as 10 mm/s. From our numerical experiences, this low speed can yield sufficiently stable results without obvious inertia effects. Moreover, the tensile strength  $N$ , mode-I fracture toughness  $G_{IC}$ , and the initial stiffness of cohesive zone  $K$  are defined in Table 1. The mesh size and predicted  $N_{min}$  using Eq. (17) are listed in Table 2 when  $E_{polymer} = 3.0$  GPa and  $N_c = 3$  (three elements in softening zone). Also, it should be noted that for the quasi-static examples in Sections 3.1 and 3.2, to speed up the computations, a one-step linear static analysis is first performed up to a proper loading level before the happening of damages. Then the computations are switched into the explicit time integration scheme. Also,  $\alpha = 0$  in Fig. 3 is constantly used in all examples.

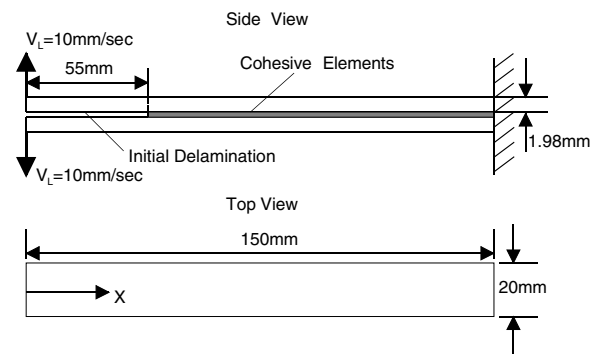


Fig. 5. Geometry of a  $[0^\circ/0^\circ]$  DCB problem.

Table 1  
Properties of cohesive element

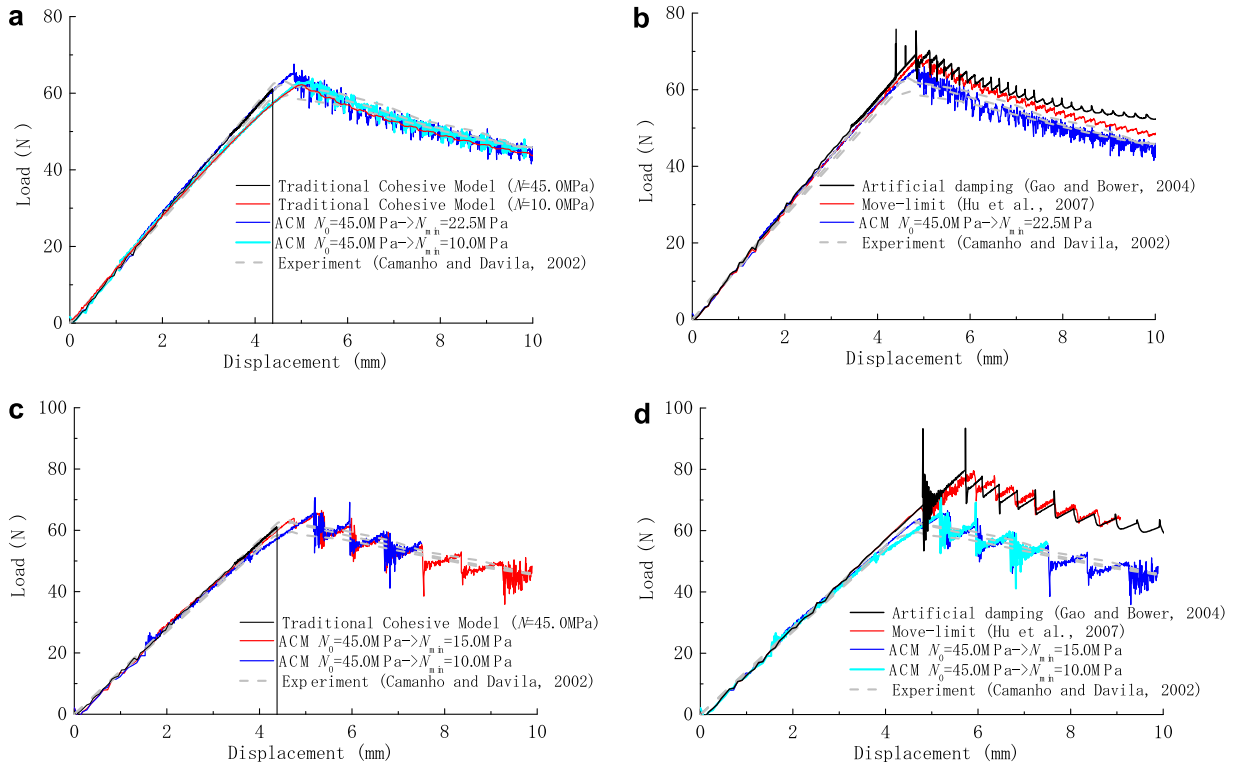
$N_0$ (MPa)	$K_0$ (N/mm <sup>3</sup> )	$G_{IC}$ (kJ/m <sup>2</sup> )	$\delta_m^0$ (mm)	$\delta_m^f$ (mm)
45	$3.0 \times 10^4$	0.378	0.0015	0.0119

Table 2  
Mesh size and predicted  $N_{min}$  in Eq. (17)

Mesh size, $R_n$ (mm)	Initial $N_0 \rightarrow N_{min}$ (MPa)
1.0	45.0 $\rightarrow$ 22.5
2.0	45.0 $\rightarrow$ 15.0

The various results are shown in Fig. 6 for two kinds of cohesive mesh sizes. First, the comparison of the results of traditional cohesive element, ACM and experiment (Camanho and Davila, 2002) is shown in Fig. 6(a) for the mesh size of 1 mm. From it, we can find that when the practical interface strength is used in the traditional cohesive model, i.e., 45.0 MPa, the result of traditional cohesive model has a sudden stop and the computation is forcefully terminated due to very strong numerical instability. With the decrease of interface strength to 10.0 MPa in the traditional model, the result is very stable, however, the slope of loading curve before the peak load is obviously lower than those of experimental ones (Camanho and Davila, 2002). For the results of ACM, when  $N_{min}$  is 22.5 MPa predicted by Eq. (17), very good result can be obtained by comparing with the experimental ones. However, when  $N_{min}$  is taken as 10.0 MPa in ACM, the same result as that of traditional cohesive model of the same interface strength is obtained. In Fig. 6(b), the results of the artificial damping (Gao and Bower, 2004) and the move-limit technique (Hu et al., 2007a) for stabilizing the numerical computations are plotted. From this figure, we can find that both techniques work stably, however, the peak loads predicted by these techniques are slightly higher than the experimental ones. When the mesh size is 2 mm, from Fig. 6(c), it can be found that the traditional cohesive element cannot track the loading–displacement history due to a sudden stop. The results of ACM for two values of  $N_{min}$  are good although the oscillation is more significant compared with those of 1 mm mesh size. Also, the slope of loading curve of ACM using 15 MPa as  $N_{min}$ , which is predicted by Eq. (17), is closer to the experimental results compared with that of ACM using 10 MPa as  $N_{min}$ . In Fig. 6(d), we can find that the results of the artificial damping (Gao and Bower, 2004) and the move-limit (Hu et al., 2007a) yield much higher peak loads than the experimental ones. By comparing with Fig. 6(b) for the case of 1 mm mesh size, we can find that with the increase of mesh size, the error in peak loads increases too in these two methods (also see the work by Goncalves et al., 2000). Naturally, this phenomenon is not caused by the above two techniques (Gao and Bower, 2004; Hu et al., 2007a). The reason is from the employed linear cohesive elements. For a cohesive elements located at the crack tip, the distribution of the relative displacements within one element is linear. If the elemental size is too large, this distribution of the relative displacements cannot reflect the real one in the crack tip area, which leads to the higher external peak load. However, in Fig. 6(d), the errors in the peak load of ACM are much smaller than those predicted by the stabilization techniques (Gao and Bower, 2004; Hu et al., 2007a) due to the proper decrease of interface stiffness. From the above discussions, we can find that ACM can yield very good results from the aspects of the peak load and the slope of loading curve if  $N_{min}$  is properly defined.

The comparison of results obtained from the different mesh sizes is illustrated in Fig. 7. In this figure, it should be noted that for the case of mesh size of 0.25 mm, the conventional cohesive model can produce the stable and converged results. Only for the mesh sizes of 1 and 2 mm, the present ACM is employed. From this figure, it can be found



**Fig. 6.** Comparison of different results of DCB problem. (a) Results of traditional cohesive element, ACM and experiments (mesh size  $R_n = 1\text{ mm}$ ). (b) Results of stabilizing techniques (Gao and Bower, 2004; Hu et al., 2007), ACM and experiments (mesh size  $R_n = 1\text{ mm}$ ). (c) Results of traditional cohesive element, ACM and experiments (mesh size  $R_n = 2\text{ mm}$ ). (d) Results of stabilizing techniques (Gao and Bower, 2004; Hu et al., 2007), ACM and experiments (mesh size  $R_n = 2\text{ mm}$ ).

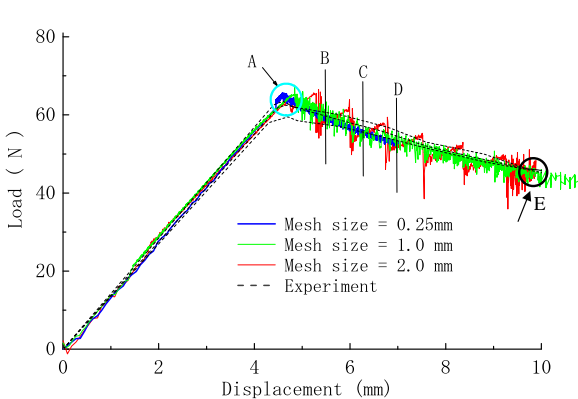


**Fig. 7.** Comparison of load histories of different mesh sizes.

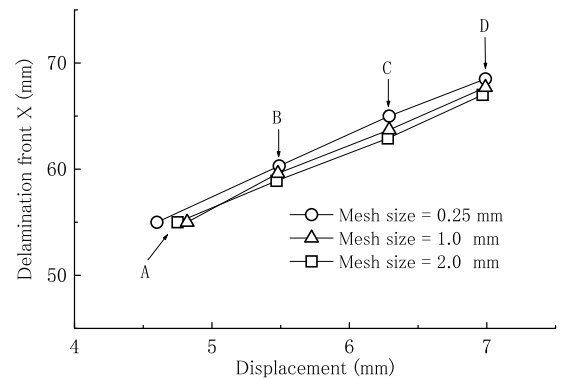


**Fig. 8.** Comparison of positions of delamination tips of different mesh sizes.

that the different mesh sizes result in almost the same loading curves. For the different stages shown in Fig. 7, i.e. A–D, the delamination tip positions for various mesh sizes are shown in Fig. 8, which demonstrates that the delamination propagation speeds are almost the same for various mesh sizes. Also, the softening zone sizes corresponding to the different mesh sizes are shown in Fig. 9. From it, we can find that, naturally, the softening zone tends to be wider as the mesh size increases and the corresponding lowest interface strength  $N_{\min}$  decreases. However, the softening zone keeps constant as the delam-

ination propagates. With the reasonable  $N_{\min}$ , the increase in softening zone size due to larger mesh size does not influence the load history and delamination size significantly. Finally, the correct and typical thumbnail delamination shape at the point E in Fig. 7 is shown in Fig. 10.

### 3.2. Verification of GFRP plate under transverse quasi-static load

A square  $[0^\circ/90^\circ/0^\circ]$  GFRP plate (Kamiya et al., 1998) is analyzed using the proposed method. The plate is shown in

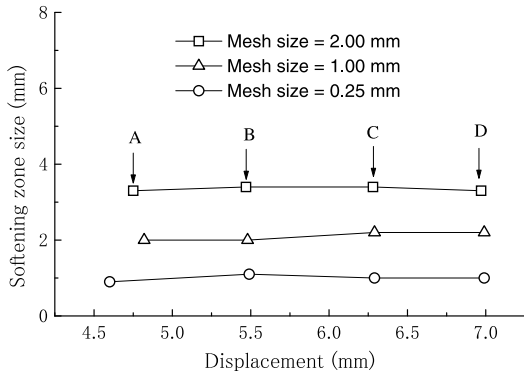


Fig. 9. Comparison of softening zone sizes of different mesh sizes.

Fig. 11. The material properties are:  $E_1 = 37.9$  GPa,  $E_2 = E_3 = 9.67$  GPa,  $G_{12} = G_{23} = G_{31} = 3.72$  GPa,  $\nu_{21} = 0.0855$ ,  $\nu_{32} = 0.4$ ,  $\nu_{13} = 0.296$  and  $\rho = 1620$  kg/m<sup>3</sup>. The interface strengths are:  $N_0 = 24$  MPa,  $N_{min} = 20$  MPa,  $S_0 = T_0 = 42.7$  MPa,  $S_{min} = T_{min} = 35.3$  MPa,  $G_{IC} = 0.24$  kJ/m<sup>2</sup>,  $G_{IIC} = G_{IIIC} = 0.64$  kJ/m<sup>2</sup>. Due to symmetry of this problem, only one quarter of plate is modeled as shown in Fig. 11. Furthermore, to reduce the computational cost, the cohesive

elements are only inserted into the lower interface between 90° and 0°, since from the experimental observation there is no obvious delamination at the upper interface. The strength parameters of GFRP material (Hu et al., 2007a) for evaluating the in-plane damages and the updating scheme of in-plane stiffness are adopted.

In the analysis, the applied load is modeled by a uniformly distributed pressure on 0.5 mm × 0.5 mm central square area of the quarter plate. For the relation between the applied load and the central deflection of plate, the numerical and experimental results (Kamiya et al., 1998) are shown in Fig. 12. The result of the move-limit method (Hu et al., 2007a) is also plotted in Fig. 12 for comparison. In this case, it can be found that both methods yield very good results compared with experimental one. At the point A, the matrix cracking happens, which leads to a small drop of applied force. At points B and C shown in Fig. 12, the numerically obtained delaminations at the lower interface, i.e., 90°//0° are shown in Fig. 13(a) and (b). Moreover, the experimental result at the point C (Kamiya et al., 1998) is shown in Fig. 13(c). Comparison between Fig. 13(b) and Fig. 13(c) reveals that the numerical delamination is in a very good agreement with the experimental one. The peanuts shape delamination is a typical pattern for this kind of cross-ply laminates.

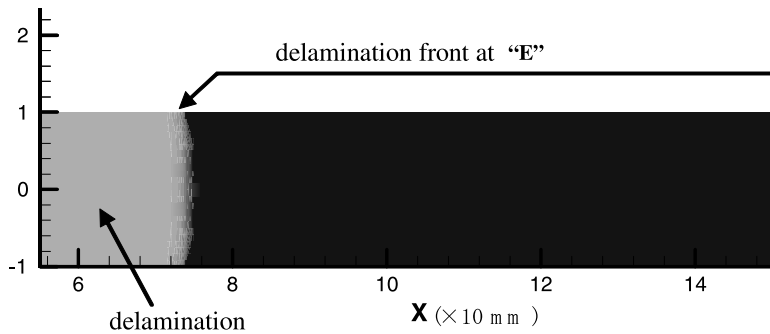


Fig. 10. Delamination shape at the point E in Fig. 7.

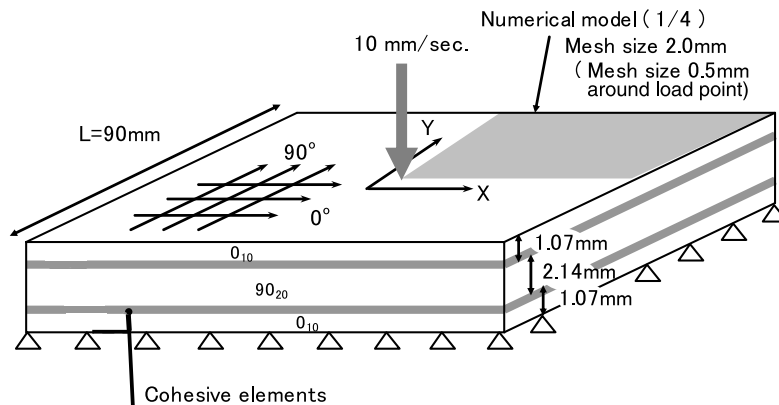
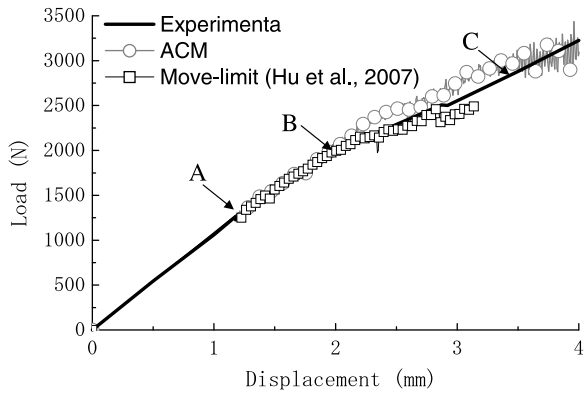


Fig. 11. Schematic view of a square GFRP cross-ply plate under central transverse load.



**Fig. 12.** Comparison between the experimental and numerical results of displacement vs. load.

### 3.3. Verification of CFRP plate under transverse low-velocity impact load

#### 3.3.1. Low-velocity impact test

The third example is a low-velocity impact problem, and the experiments were performed by the present authors using a weight-drop impact test machine of Dynatup 9250HD. The experimental setup is shown in Fig. 14. The specimens were prepared according to the SACMA standard of CAI test. As shown in Fig. 15, a quasi-isotropic CFRP laminated plate of 32 plies as  $[(45^\circ/0^\circ/-45^\circ/90^\circ)_4]_s$  is put on the bottom frame with four fixed points. This plate is impacted by an impacting body of a lower semi-spherical shape and the mass of 4.6 kg. As shown in Table 3, we have performed eight tests for four impact energy levels, i.e. 3.0, 4.8, 6.0 and 7.2 J. Two tests have been carried out for each energy level. When the impact energy is 3.0 J, there is no impact-induced damage in Table 3. It is interesting to note that for the impact energy of 4.8 J, the damages occur in one specimen, but does not occur in another one. Therefore, the impact energy of 4.8 J can be thought of as the threshold of impact energy, which induces the possible damages in CFRP laminates. When the impact energy is higher than 4.8 J, e.g., 6.0 and 7.2 J, there are obvious impact-induced damages in four specimens. The ultrasonic results of specimen after impact for these two energy levels will be shown later. From the ultrasonic results, it can be found that the damage area in the impacted side is

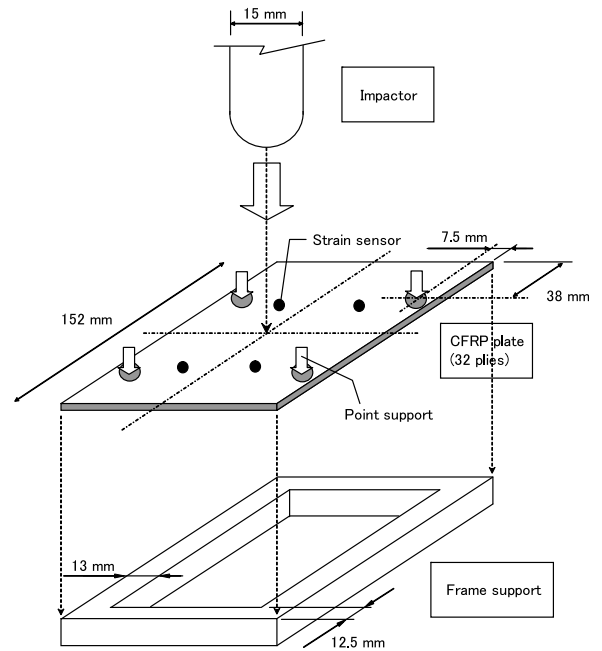


**Fig. 14.** Schematic view of impact test.

larger than that of the opposite side of impact. At the cross-sections of specimen, the approximate delamination distribution along the thickness direction is shown in Fig. 16. The damages near the top and bottom surfaces within three plies can be practically observed using ultrasonic inspections. The internal damages are speculated. Although the extent of the delamination is not quantified in this figure, it increases with depth and a typical conical shape is obtained with the top surface located close to the impact point.

#### 3.3.2. Numerical modeling of low-velocity impact test

First, in our numerical model, the following material properties of lamina of CF/epoxy are used:  $E_1 = 135.0$  GPa,  $E_2 = E_3 = 10.0$  GPa,  $G_{12} = G_{13} = 5.50$  GPa,  $G_{23} = 4.50$  GPa,  $\nu_{12} = 0.0183$ ,  $\nu_{13} = 0.45$ ,  $\nu_{23} = 0.25$ ,  $\rho = 1489$  kg/m<sup>3</sup>. Also, the properties for damage simulations are listed as follows:  $N_0 = 85.0$  MPa,  $S_0 = T_0 = 106.0$  MPa,  $N_{\min} = 76.5$  MPa,  $S_{\min} = T_{\min} = 95.4$  MPa,  $G_{IC} = 0.5$  kJ/m<sup>2</sup>,  $G_{IIC} = G_{IIIC} = 1.0$  kJ/m<sup>2</sup>. To

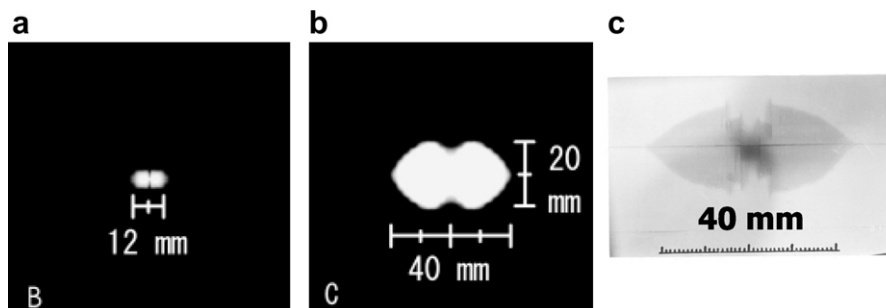


**Fig. 13.** Delamination shapes at lower interface at points B and C in Fig. 12. (a) Numerical (point B), (b) numerical (point C), (c) experimental (point C, see Kamiya et al., 1998).

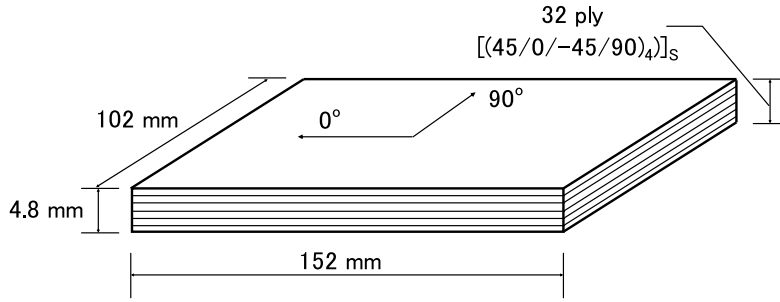


Fig. 15. Specimen of 32 plies quasi-isotropic CFRP plates.

Table 3  
Results of impact tests for various impact energies

Case no.	Impact energy (J)	Damage
1	3.0	None
2	3.0	None
3	4.8	None
4	4.8	Damaged
5	6.0	Damaged
6	6.0	Damaged
7	7.2	Damaged
8	7.2	Damaged

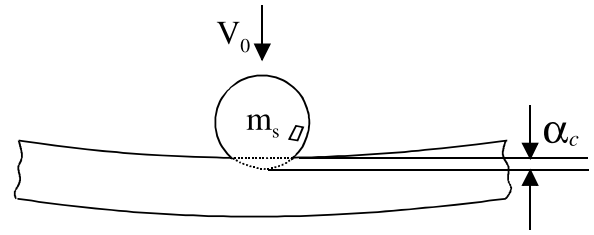


Fig. 17. Contact model between a rigid ball and laminates.

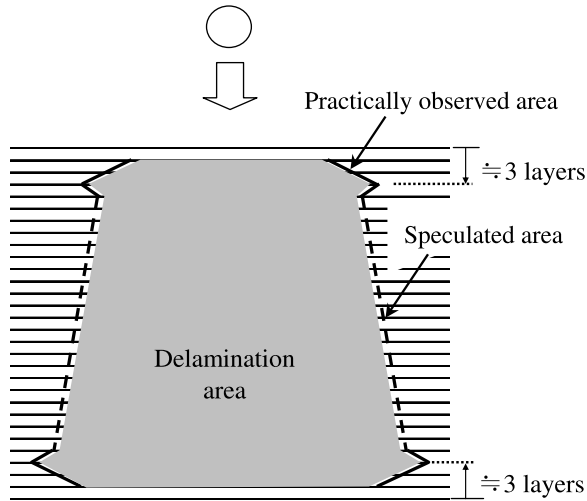


Fig. 16. Schematic view of delamination distribution along thickness direction in experimental specimen.

deal with the possible the in-plane damages, the strength parameters of CFRP material (Hu et al., 2007a) are adopted. However, the fiber breakage has not been considered in the present model since from the experimental observations, no fiber breakage has been identified. Also, as shown in Fig. 17 for the indentation  $\alpha_c$  between a ball and a laminate, the modified Hertz contact law (Tan and Sun, 1985) is employed to deal with the contact between the ball and the laminate, which is listed as follows:

- Loading

$$F = \kappa \alpha_c^{1.5}, \quad 0 < \alpha_c \leq \alpha_m \quad (18)$$

Table 4  
Constants used in modified Hertz contact model

Indentation constants
$\beta = 0.094, \alpha_{cr} = 0.1667 \text{ mm}, \kappa = 1.423 \times 10^6 \text{ N/cm}^{1.5}, q = 2.5$

- Unloading

$$F = F_m \left( \frac{\alpha_c - \alpha_0}{\alpha_m - \alpha_0} \right)^q \quad (19)$$

where  $\alpha_m$  is the maximum indentation in the loading stage,  $F_m$  is the maximum contact load before unloading, and  $\alpha_0$  is permanent indentation and defined as

$$\alpha_0 = \begin{cases} \beta(\alpha_m - \alpha_{cr}) & \text{if } \alpha_m > \alpha_{cr} \\ 0 & \text{if } \alpha_m < \alpha_{cr} \end{cases} \quad (20)$$

where  $\beta$  and  $\alpha_{cr}$  are experimental constants.  $\kappa$  and  $q$ , which depend on the shape of the ball and material properties of the laminate and the ball. All of these parameters are taken from the work of Tan and Sun (1985), and listed in Table 4.

Some efforts have been performed to reduce the computation cost when modeling this complex problem with 32 plies. The whole plate needs be modeled due to the existence of  $\pm 45^\circ$  plies. As shown in Fig. 18, the plate is divided into three portions. In the central area of  $35 \text{ mm} \times 35 \text{ mm}$ , along the thickness direction, 32 brick elements at 32 plies are placed plus 30 cohesive elements at 30 interfaces since the maximum size of delaminations is smaller than  $30 \text{ mm} \times 30 \text{ mm}$  from experimental observations. Also, at the interface of middle two plies  $90^\circ/90^\circ$ , there is no need to insert cohesive interface element. The

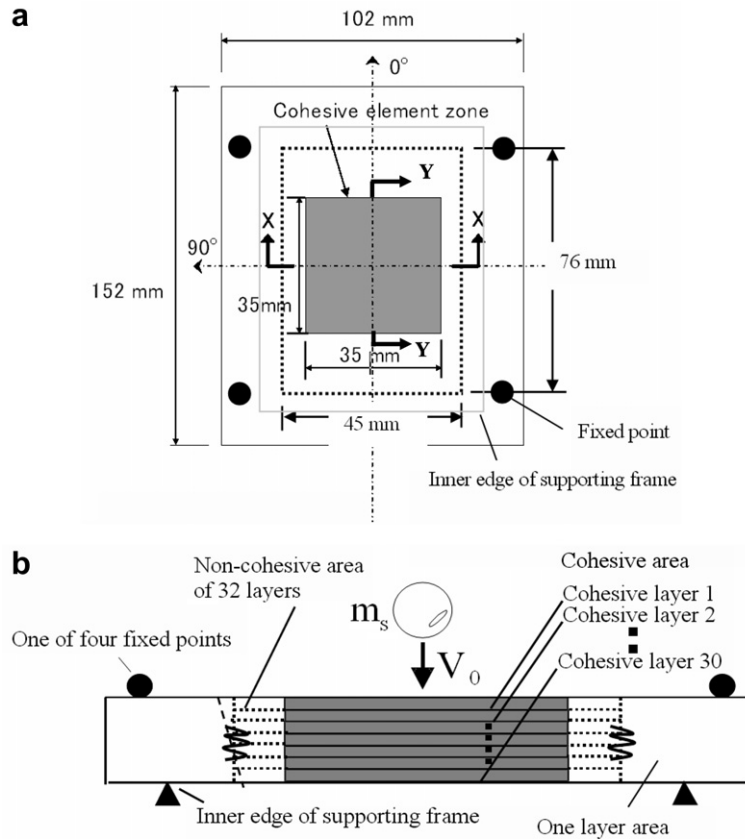


Fig. 18. Schematic view of finite element discretization. (a) Top view, (b) side view.

mesh size in this central area is  $2.5 \text{ mm} \times 2.5 \text{ mm}$ . In general, there is an enormously important problem, i.e., the happening of acoustic emission from the impact load and the associated damaging events, which can be used to locate the impact position and to monitor the damage happening (Mal et al., 2003a,b). To reflect these acoustic waveforms in the numerical model, whose central frequency is usually lower than 120 kHz (Mal et al., 2003a,b), the element size should be sufficiently small relating to the wavelength. In general,  $A_0$  wave mode in Lamb waves possesses the shortest wavelength, at around 100 kHz, which ranges from 1.5 to 2.5 cm depending the thickness and stack sequence of CFRP plates. Therefore, the size of present element, i.e.,  $2.5 \text{ mm} \times 2.5 \text{ mm}$ , is sufficiently small to reflect these acoustic waveforms since the present element holds a linear strain and stress fields (Cao et al., 2002). In the outer region marked by dotted lines in Fig. 18, the cohesive elements at 30 interfaces are omitted, and only 32 brick elements at 32 plies are placed along the thickness direction. In the outermost area, only one brick element along the thickness direction is placed. The reason is that the deformation behaviors and damage characteristics of laminates induced by low-velocity impacts are dominated by the local area under the ball. The distant structural information far away from impacted area is not important (Li et al., 2002a,b). The equivalent material properties of the outermost one layer are determined from

the comparison of first three natural frequencies of a cantilevered specimen, which are obtained from vibration tests and numerical computation of a one-layer model, respectively. In Fig. 18, with the assumption of linear distribution of in-plane displacements along the thickness direction, some strong springs are inserted at the boundary between the 32-layer region and the 1-layer region to enforce the continuity of displacements. Finally, the total number of elements including the cohesive elements is 24,696. The contact force between the ball and CFRP laminates is simulated by a distributed load applied on a  $4 \text{ mm} \times 4 \text{ mm}$  central square area of plate since it is observed that there is an approximate circular unrecoverable indentation area of radius of around  $2.0 \text{ mm} \sim 2.5 \text{ mm}$  on specimens after impacts.

### 3.3.3. Comparison of numerical and experimental results

First, for the case of 3.0 J without impact damages, the impact force histories obtained numerically and experimentally are shown in Fig. 19(a). This figure illustrates that the numerical result agree with two experimental results very well. In numerical simulations, no damages have been identified too. For the cases of 6.0 and 7.2 J, the comparisons of the impact force histories are demonstrated in Fig. 19(b) and (c), respectively. From these figures, it can be found that the numerical results agree with the experimental ones very well. One can observe that the repeat-

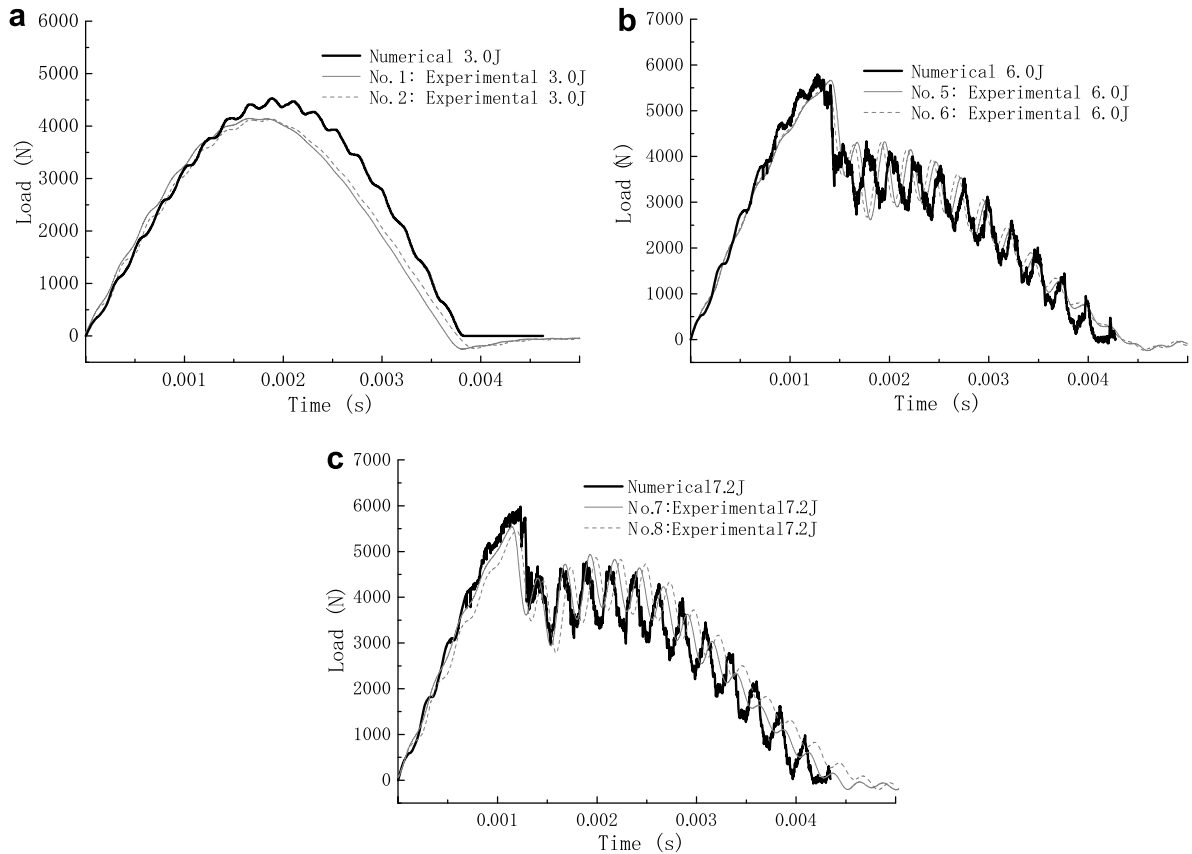


Fig. 19. Comparison of numerical and experimental results (impact force). (a) 3.0 J, (b) 6.0 J, (c) 7.2 J.

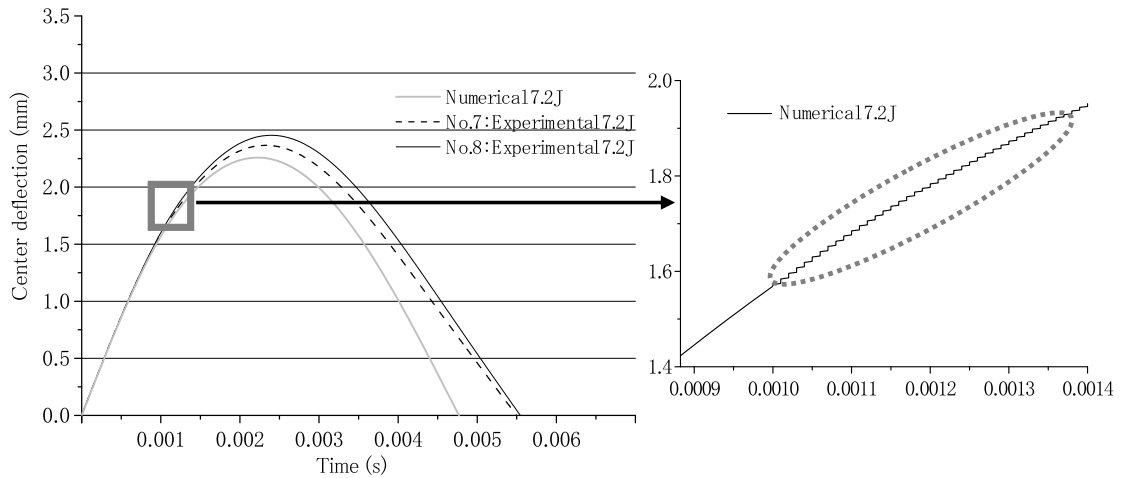


Fig. 20. Comparison of numerical and experimental results (deflection, 7.2 J).

ability of two experimental results is acceptable, considering the shape of these curves and force levels for the damaged samples. For the features of impact force history, after the peak load, there is a sudden drop in the force history. After this drop, the impact force decreases gradually. From

Fig. 19(c), we can find that the impact force of 7.2 J is basically similar to that of 6.0 J in Fig. 19(b). However, after the sudden drop from the peak load, the impact load of 7.2 J does not decrease immediately as that of 6.0 J. In contrast, there is a platform where the impact load keeps almost

constant. After this platform, the impact load decreases gradually. The numerical result reproduces this feature very well compared with the experimental one in Fig. 19(c).

The comparison of numerical and experimental deflections is demonstrated in Fig. 20 for the case of 7.2 J. It can be found that the numerical result agrees with two experimental ones very well. Three deflections seem to be very smooth in the left figure of Fig. 20. However, if we enlarge a local region of the numerical deflection as shown in the right figure of Fig. 20, we can find that the deflection is very smooth before 0.001 s, i.e., corresponding to the stage before the peak load in Fig. 19(c). It means that there is no significant damaging extent before the peak load. However, after 0.001 s, there are obvious and continuous oscillations of plate deflection in the right figure of Fig. 20,

which corresponds to the unloading stage in Fig. 19(c). In this stage, the delamination and other damaging extents extend continuously which cause the number of high-frequency acoustic emission events to increase dramatically as shown experimentally by Mal et al. (2003a,b). In general, corresponding to the contact load, few isolated acoustic signals also occur, however, whose main frequency content is much lower than those of the continuous acoustic events caused by damaging events. Usually, the amplitude of plate oscillations caused by the acoustic wave propagation is very small as shown in the right figure of Fig. 20 (also see, Hu et al., 2007b,c).

To illustrate the delaminations at various interfaces, two sections, i.e. X–X and Y–Y sections are defined in Fig. 18(a). A sketch of the delaminations at various interfaces obtained numerically is shown in Fig. 21 for 6.0 and 7.2 J.

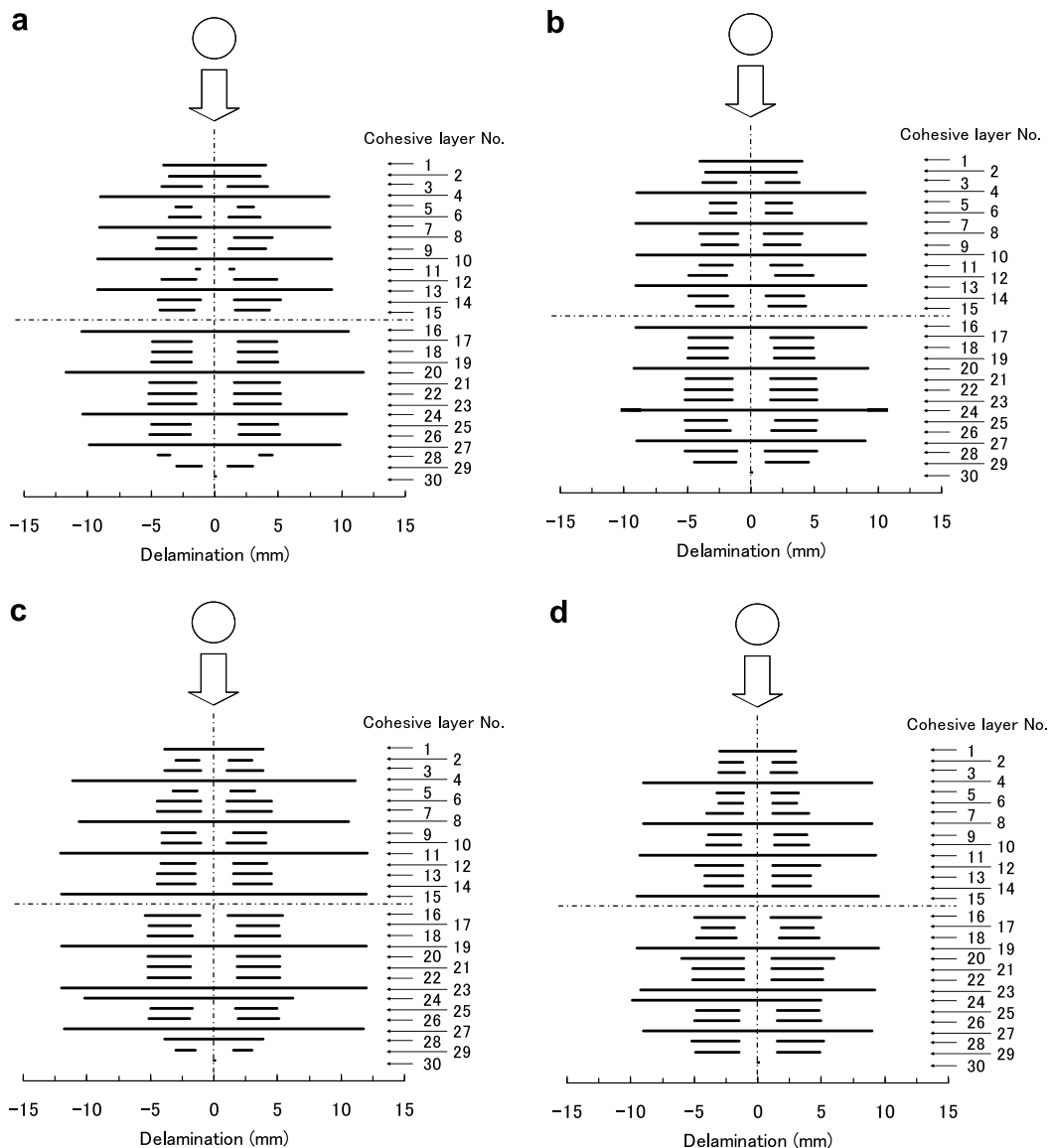


Fig. 21. Delaminations at various interfaces. (a) X–X section (6.0 J), (b) Y–Y section (6.0 J), (c) X–X section (7.2 J), (d) Y–Y section (7.2 J).

By comparing these results with that shown in Fig. 16, we can find that the present numerical model can capture the main features of delamination distribution along the thickness direction. Furthermore, the delaminations on the side of impact and the opposite side of impact, which are obtained from numerical computations and ultrasonic inspections of specimens, respectively, are shown in Figs. 22 and 23. In these figures, for the numerically obtained delaminations on the side of impact, the delaminations between the first and tenth interfaces are plotted. Meanwhile, for the delaminations on the opposite side of impact, the delaminations between the 21st and 30th

interfaces are plotted. From these figures, we can find that the numerically obtained delaminations agree with experimental ones very well although the maximum sizes of delaminations are slightly smaller than those of experimental ones at the opposite side of impact. Also, compared with the experimental results, the numerically obtained delamination shape is more unsymmetrical. As to the computational instability problem, after investigating various cases, it is very interesting to find that the computational process tends to be more instable as the impacting speed of the ball decreases at the same impact energy level. Naturally, the present ACM can still be employed to avoid this

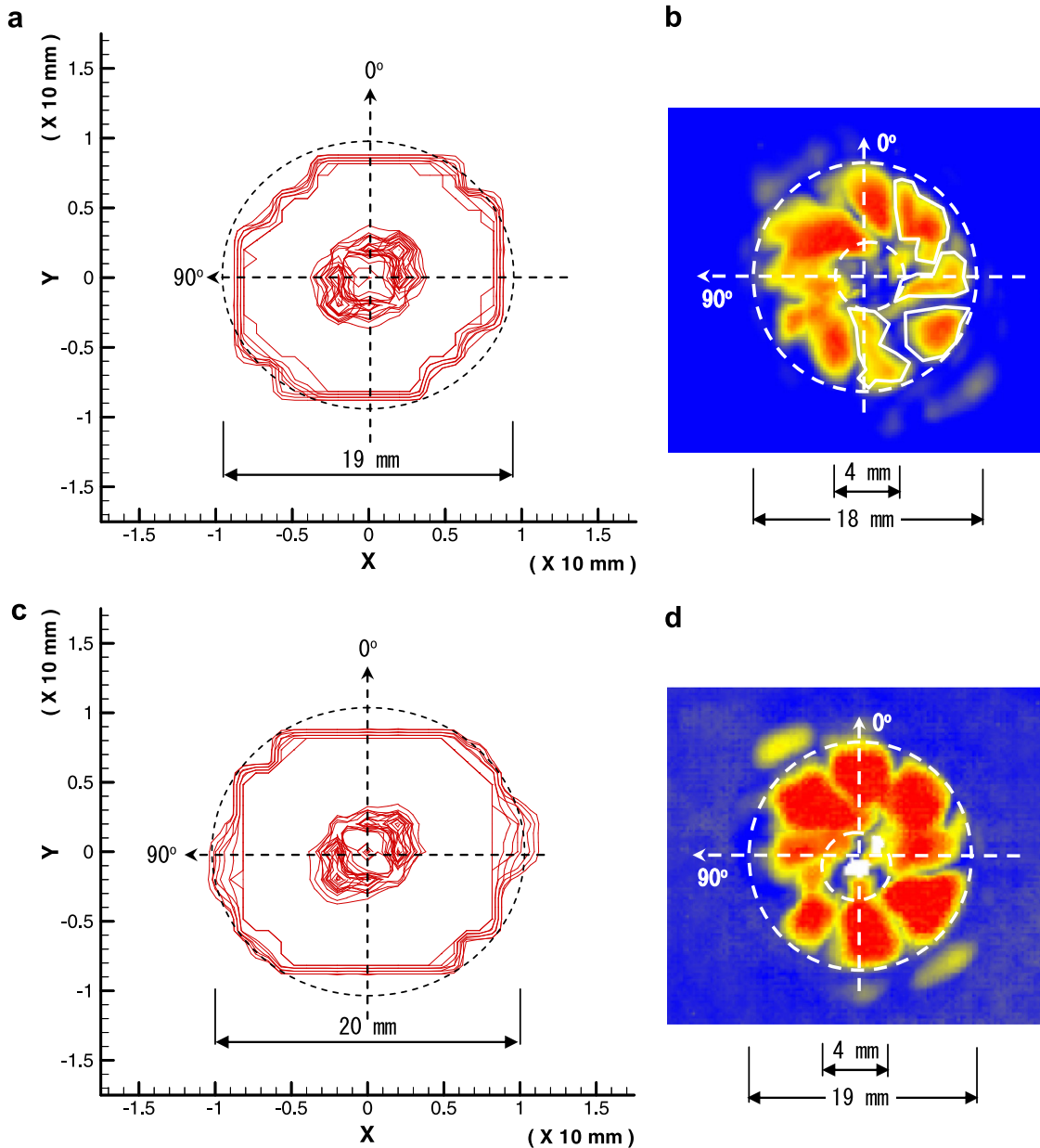
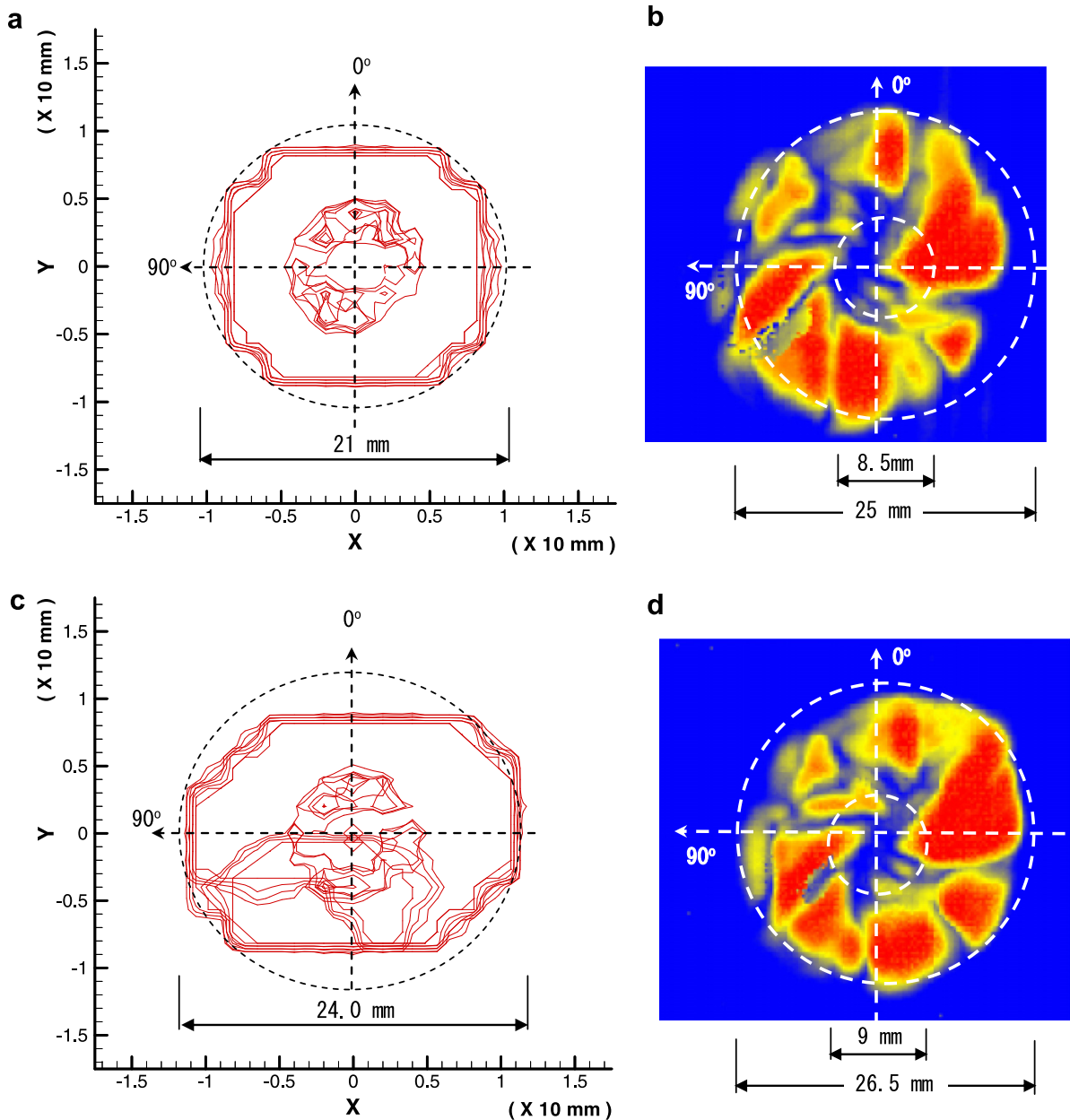


Fig. 22. Comparison of delaminations obtained from FEM and experiments at the side of impact on specimen. (a) Numerical (6.0 J), (b) experimental (6.0 J), (c) numerical (7.2 J), (d) experimental (7.2 J).



**Fig. 23.** Comparison of delaminations obtained from numerical computations and experiments at the opposite side of impact on specimen. (a) Numerical (6.0 J), (b) experimental (6.0 J), (c) numerical (7.2 J), (d) experimental (7.2 J).

instability. For higher impacting speeds, the numerical instability is not obvious.

#### 4. Conclusions

In this research, we have put forward a novel cohesive model for simulating the delamination propagations in composite laminates under transverse loads. This cohesive model is implemented in the explicit time integration scheme with a powerful 3D finite element. A DCB problem is employed to analyze the characteristics of the present cohesive model. From the results, it can be found that the

present model can yield stable computational results, and can reduce the errors in the peak load caused by comparatively coarse meshes. In fact, with the guarantee of the acceptable accuracy, the cohesive elemental size in our model can be enlarged by around 5–10 times larger than that used in the traditional cohesive model. Moreover, to analyze the complex damages happening in laminates, a stress-based criterion is incorporated into our numerical model for predicting various in-plane damages, such as matrix cracks, fiber breakage, etc. Finally, two experimental examples of laminated plates under transverse quasi-static and low-velocity impact loads are employed

to illustrate the validity of the present approach. It can be found that the present numerical model can successfully capture the main features of complex damage phenomena in composite laminates under transverse loads.

### Acknowledgements

This work is partly supported by the Award from Research Fund for Overseas Chinese Young Scholars from National Natural Science Foundation of China (No. 50728504), Grand-in-Aid for Scientific Research (No. 19360045) from the Japanese Ministry of Education, Culture, Sports, Science and Technology, and Natural Science Foundation Project of CQ CSTC to N.H.

### References

- Brewer, J.C., Lagace, P.A., 1988. Quadratic stress criterion for initiation of delamination. *Journal of Composite Materials* 22, 1141–1155.
- Camacho, G.T., Ortiz, M., 1996. Computational modelling of impact damage in brittle materials. *International Journal of Solids and Structures* 33, 2899–2938.
- Camanho, P.P., Davila, C.G., 2002. Mixed-mode decohesion finite elements for the simulation of delamination in composite materials. *NASA/TM-2002-211737*.
- Cao, Y.P., Hu, N., Lu, J., Fukunaga, H., Yao, Z.H., 2002. A 3D brick element based on Hu-Washizu variational principle for mesh distortion. *International Journal of Numerical Methods in Engineering* 53, 2529–2548.
- Chang, F.K., Chang, K.A., 1987. A progressive damage model for laminated composite containing stress concentrations. *Journal of Composite Materials* 21, 834–855.
- Davies, G.A.O., Zhang, X., 1995. Impact damage prediction in carbon composite structures. *International Journal of Impact Engineering* 16, 149–170.
- Gao, Y.F., Bower, A.F., 2004. A simple technique for avoiding convergence problems in finite element simulations of crack nucleation and growth on cohesive interfaces. *Modelling and Simulation in Materials Science and Engineering* 12, 453–463.
- Geubelle, P.H., Baylor, J.S., 1998. Impact-induced delamination of composites: a 2D simulation. *Composites Part B* 29B, 589–602.
- Goncalves, J.P.M., De Moura, M.F.S.F., De Castro, P.M.S.T., Marques, A.T., 2000. Interface element including point-to-surface constraints for three-dimensional problems with damage propagation. *Engineering Computations* 17, 28–47.
- Hou, J.P., Petrinic, N., Ruiz, C., Hallet, S.R., 2000. Prediction of impact damage in composite plates. *Composites Science and Technology* 60, 273–281.
- Hou, J.P., Petrinic, N., Ruiz, C., 2001. A delamination criterion for laminated composites under low-velocity impact. *Composites Science and Technology* 61, 2069–2074.
- Hu, N., Zemba, Y., Fukunaga, H., Wang, H.H., Elmarakbi, A.M., 2007a. Stable numerical simulations of propagations of complex damages in composite structures under transverse loads. *Composites Science and Technology* 67, 752–765.
- Hu, N., Fukunaga, H., Kameyama, M., Roy Mahapatra, D., Gopalakrishnan, S., 2007b. Analysis of wave propagation in beams with transverse and lateral cracks using a weakly formulated spectral method. *Journal of Applied Mechanics (ASME)* 74, 119–127.
- Hu, N., Wang, H.H., Yan, B., Fukunaga, H., Roy Mahapatra, D., Gopalakrishnan, S., 2007c. The partition of unity finite element method for elastic wave propagation in Reissner–Mindlin plates. *International Journal of Numerical Methods in Engineering* 17, 1451–1479.
- Kamiya, S., Sekine, H., Yagishita, Y., 1998. Computational simulation of interlaminar crack extension in angle-ply laminates due to transverse loading. *Journal of Composite Materials* 32, 744–765.
- Li, C.F., Hu, N., Yin, Y.J., Sekine, H., Fukunaga, H., 2002a. Low-velocity impact-induced damage of continuous fiber-reinforced composite laminates. Part I. An FEM numerical model. *Composites Part A* 33, 1055–1062.
- Li, C.F., Hu, N., Chen, J.G., Fukunaga, H., Sekine, H., 2002b. Low-velocity impact-induced damage of continuous fiber-reinforced composite laminates. Part II. Verification and numerical investigation. *Composites Part A* 33, 1063–1072.
- Mal, A., Shih, F., Banerjee, S., 2003. Acoustic emission waveforms in composite laminates under low velocity impact. In: Kundu, T. (Ed.), *Proceedings of the SPIE Conference on NDE for Health Monitoring and Diagnostics*, 5047, pp. 1–12.
- Mal, A., Shih, F., Prosser, W., 2003b. Lamb waves from impact damage in composite plates. *Instrumentation Measure Metrologies, Special Issue on Ultrasonic Methods for Material Characterization* 3, 11–37.
- Mi, Y., Crisfield, M.A., Davis, G.A.O., 1998. Progressive delamination using interface element. *Journal of Composite Materials* 32, 1246–1272.
- Nishikawa, M., Okabe, T., Takeda, N., 2007. Numerical simulation of interlaminar damage propagation in CFRP cross-ply laminates under transverse loading. *International Journal of Solids and Structures* 44, 3101–3113.
- Reddy Jr., E.D., Mello, F.J., Guess, T.R., 1997. Modeling the initiation and growth of delaminations in composite structures. *Journal of Composite Materials* 31, 812–831.
- Riks, E., 1979. An incremental approach to the solution of snapping and buckling problems. *International Journal of Solids & Structures* 15, 529–551.
- Segurado, T.M.J., Llorca, C.T.J., 2004. A new three-dimensional interface finite element to simulate fracture in composites. *International Journal of Solids and Structures* 41, 2977–2993.
- Tan, J.T.M., Sun, J.C.T., 1985. Use of statistical indentation laws in the impact analysis of laminated composite plates. *Journal of Applied Mechanics* 52, 5–12.
- Xu, X.P., Needleman, A., 1994. Numerical simulations of fast crack growth in brittle solids. *Journal of Mechanics and Physics of Solids* 42, 1397–1434.
- Zheng, S., Sun, C.T., 1995. A double-plate finite-element model for the impact-induced delamination problem. *Composites Science and Technology* 53, 111–118.